Full-scale Nonlinear Analysis of LHL Ga As IMPATT Amplifiers

SAID H. IBRAHIM
Computer and Electronics Engineering Department.
King Faisal University
Al-Ahsa P.O. Box 400 Tel. 0096635800000
K.S.A.
saidhassan1@yahoo.com

HOSNY A. AL-MOTAAFY
Prof., Higher Technological Institute, Tenth of Ramadan , Cairo, Egypt

Abstract: The analysis of LHL Ga As IMPATT Diode structure has been developed on the basis of IMPATT nonlinear model. The paper presents a detailed analysis of the effect of peak value of the microwave signal and the operating conditions on the performance of GaAs IMPATT amplifiers. It is indicated that the variation of peak RF voltages gives rise to three modes of operation (conventional mode and two high-efficiency modes) . During the high-efficiency modes, the induced current has one or two additional peaks at the proper phase angles in the RF cycle due to the bunching and acceleration of the avalanche-generated packet of electrons. The diode conductance and the generated RF power increase sharply during the high-efficiency operation. Important conclusions concerning the effects of the dc bias current and operating frequency on the performance of this device are drawn. The results presented here are obtained using a full-scale computer simulation program that takes fully into account all the physical effects pertinent to the IMPATT diode operation .They will help optimize the Ga As IMPATT structure and its operating conditions.

Key Words: Computational Microstrip Circuit Design, Microwave Circuits, Computer Aided Design

1 Introduction

It is known that the low-high-low (LHL) Ga As IMPATT diodes give efficiencies that exceed the maximum theoretical efficiency predicted for IMPATT diodes [1-13]. The purpose of this paper is to shed further light on the operation and performance of LHL Ga As IMPATT diode. Since the LHL structure is considered to be the optimum IMPATT structure, all the results presented here will be for this type [6-13]. These results are obtained using a modified version of the full-scale computer-simulation program developed by the authors [14-17]. This program takes fully into account the nonlinear model that contains the differential equations for the carrier concentrations (continuity equations) , current density equation, the dependence of the ionization Coefficients on the field, and the electric field distribution in the semiconductor structure (Poisson equation) [17-19] and all the physical effects pertinent to IMPATT operation. Hence, these results can be considered accurate and reliable. The behavior of the charge carriers and their interaction with the electric field are analyzed and explained. The dependence of the performance on the peak RF voltage, dc-bias current and frequency is explained and interpreted.

In order to get better insight into the operation of Ga As IMPATT two properly chosen diodes will be studied. The first one (D_1) has a low-high-low structure and its active region is n-type doped. The parameters of the n-type diode are:

- The width of the avalanche region w_a=0.4 μm
- The width of the drift region (DR) w_d=5.5 μm
- The doping density in the avalanche region $n_a=10^{15}$ cm^{-3}
- The doping density in the drift region n_d=3 x10^{15} cm^{-3}
- The size of the doing clump=1.7 x 10^{12} cm^{-2}
- The doping density in the ohmic contact n^+ and p^+=2 x 10^{17} cm^{-3} .

The second diode (D_2) has a p-tpye LHL Ga As IMPATT diode having the following parameters:

- The width of the avalanche region w_a=0.3 μm
- The width of the drift region (DR) w_d=3.0 μm
- The doping density in the avalanche region $n_a=10^{15}$ cm^{-3}

- The size of the doing clump=1.7 x 10^{12} cm^{-2}
- The doping density in the ohmic contact n^+ and p^+=2 x 10^{17} cm^{-3}

Figure 1 shows the structure, doping profile and field distribution of LHL IMPATT diode.

The amplifier whose performance will be studied is a reflection type amplifier shown in figure 2 . It comprises a circulator, a 4-terminal network, an IMPATT diode, and the load Y_L. The 4-terminal network represents the cavity or transmission line where the diode is mounted. The gain of reflection amplifier Ga is given by:

$$G_a = |\frac{(Y_c - Y_d{}^*)}{(Y_c + Y_d)}|^2$$

Or

$$G_a = \frac{P_o}{P_i} = \frac{(P_i + P_a)}{P_i} = (1 + \frac{P_a}{P_i})$$

Where: Y_c is the equivalent admittance of microwave circuit looking away from the diode at some convenient reference plane, Y_d is the admittance seen looking toward the diode from the same reference plan, * is used to indicate the complex conjugate, P_i is the input power, P_a is the power added by the diode, and P_o is the output power

The power added by the diode can be calculated from:

$$P_a = 0.5|G_d|V_{rf}{}^2$$

Where: $V_{rf} is$ the RF voltage applied across the diode, and $|G_d|$ is the absolute value of the diode conductance. It must be mentioned that G_d is negative during IMPATT operation.

2 Results

Figures 3 and 4 show the efficiency(η), the amplifier gain, the magnitude of diode conductance $|G_d|$, the RF-generated power (P_{RF}), and the amplifier output power (P_{OUT}) versus the peak value of the RF voltage (P) for the dc-bias current (J_{dc}) of 900 A/cm^2 and the frequency (F) of 8 GHz. It is seen that η increases firstly monotonically with P. Then, there is a sharper increase of η indicating a change of the mode of operation. η attains its maximum value at P=64 V. Then, η decreases sharply. It is also seen that $|G_d|$, P_{RF} , the amplifier gain, and P_{OUT} increase also sharply with P at the onset of the high-efficiency operation. Figures 5 and 6 show P_{RF} and η versus F for J_{dc} ranging from 1000 to 6000 A/cm^2. It is seen that the optimum frequency, at which η is maximum, increases with J_{dc}. Namely, the optimum frequency is 13 GHz at $J_{dc=}$1000A/cm^2 and 15 GHz at J_{dc}=6000 A/cm^2. It is also seen that the frequency at which the IMPATT diode starts to generate RF power increases with J_{dc}.

Figure 7 and 8 show η and P_{RF} versus P for J_{dc} ranging from 1000 to 3000 A/cm^2 at F=13 GHz. It is noticed that the optimum peak increases slightly with J_{dc}. Figure 9 shows η and P_{RF} versus J_{dc} at F=13 GHz and P=55 V. These results and all the other results will be interpreted physically in the following sections

3 Analysis of the Effect of the Peak RF Voltage

In order to understand the above-mentioned results, it is necessary to study the diode operation as P is varied. Fig. 10 shows the spatial distribution of the electron current (J_n) at different phase angles for P=45 V. It is evident that the diode is operating according to the conventional IMPATT mode; the avalanche-generated packet of electrons (AGP) after being generated is injected into the drift region (DR). During its motion toward the ohmic contact where they are extracted, it is slightly dispersed by the effect of diffusion. The depletion-layer width modulation (DWM) effect causes some carriers to be injected into the DR from the ohmic contact causing a negative electron current. However, this effect is not pronounced for this value of P.

Figure 11 shows the terminal voltage (V_t), the induced current (J_i) for P=63 and 64 V. Figures 12 and 13 show the J_n , and the electron density (n) for P=63 V. Figure 14 shows the electric field (E) and J_n at different phase angles (Θ) for the same value of P that essentially lies in the high-efficiency region of the diode characteristic. Hence, the diode is not operating according to the conventional IMPATT mode but according to the first high-efficiency IMPATT mode [7-12]. The behavior of the charge carriers and their interaction with the local field in the IMPATT and the resultant induced current will now be discussed.

At the start of the RF cycle, some of the carriers that are generated in the previous RF cycle are still being extracted at the left end of the DR. This gives rise to the induced current found at the beginning of the cycle. At Θ=90°, only a negligible amount of electrons is still being extracted and J_I is minimum. Since V_t is maximum at this phase angle, E attains its highest values alongside the diode. However, the avalanche generation does not start at this phase angle since the density of carriers already existing in the avalanche region is extremely small. The avalanche generation starts to be effective after this phase angle and the (AGP) grows to attain its maximum volume at Θ=180°. causing J_i to have a peak. At this phase angle the negative half cycle

(NHC) begins , V_t starts to decrease below the dc-breakdown voltage, and the AGP of electrons is injected into the DR. Figure 12 shows this AGP during its motion towards the ohmic contact(n+)at different Θ. Figure 13 shows the electron density (normalized to 10^{15} cm^{-3}) at the same phase angles. It is seen that as the AGP is moving in the drift region at a velocity almost equal to v_s, it is slightly dispersed by the effect of diffusion. A current is induced in the external circuit because of this motion. The decrease of J_I after 180 deg. is attributed to the extraction of the minority carriers generated in the avalanche region. During the motion of the AGP it decreases the field behind it and increases it in its front. This is the space charge (SC) effect which is not significant for this value of J_{dc} . However, this effect helps reduce the drift-velocity dropping below saturation (VDBS) effect and the DWM effect . At $\Theta=234^o$., the DWM becomes effective and E drops to very small negative values near the left end of the DR. Mobile carriers will be injected from the ohmic contact into the DR contributing a current in anti-phase relationship with that induced by the AGP. Hence, J_I decreases and has a dip at $\Theta=234^o$. In other words, it can be said that an undepleted region (UR) is formed at the extremity of the DR and moves towards the AGP. For $\Theta > 261^o$, the DWM effect is reduced because of the SC effect of the AGP that is moving towards the ohmic contact. At $\Theta=270^o$., the AGP is bunched and its peak increases. In addition, it is accelerated in the DR. This is attributed to the fact that the values of E in the portion of the DR occupied by the AGP lies now in the negative-differential-mobility region (NDMR) of the velocity-field characteristic of the Ga As material [22]. In order to fulfill this condition, J_{dc} and n_d must be properly chosen [8-12]. In addition, the carriers that are injected into the DR from the ohmic contact change their direction now and move towards the ohmic contact. These effects cause J_I to increase. At $\Theta=279^o$, the bunching and acceleration of the AGP becomes more pronounced. Correspondingly, J_I attains a small peak at this phase angle. The bunching and acceleration continues for $279^o < \Theta < 297^o$, but the carriers in the front edge of the AGP start to be extracted. On the other hand, the carriers constituting the tail of the AGP are trapped by the small values of E in the middle of the DR. This effect together with the extraction of carriers causes J_I to decrease. The extraction of carriers together with the increase of V_t cause E to increase in the DR. Consequently, the AGP starts to be dispersed at $\Theta=297^o$. The extraction of carriers occurs at velocities greater than v_s . Consequently, J_I decreases sharply. As the extraction of carriers continues and V_t increases the values of E increase and are now outside the NDMR. The extraction of carriers continues at velocities equal to v_s which is smaller than the peak velocity v_p. Hence, J_I decreases less sharply. For this value of P, the extraction of carriers is not perfect causing J_I to have a large value at the end of the cycle.

Figures 11 and 15 through 17 show the results obtained when P is increased to 64 V. This is the optimum value at which the efficiency is maximum. It is seen that at $\Theta=234^o$, the situation is similar to the previous case. At this phase angle, the DWM effect becomes effective and more significant than the previous case. Hence, J_I undergoes a slightly larger dip. AT $\Theta=261^o$, the bunching and acceleration of the AGP start causing J_I to increase and to have a small peak. These two effects are now more pronounced. The electric field in front of the AGP becomes almost zero and the carriers in the undepleted region are trapped. At $\Theta=270^o$, the bunching and acceleration continue but the AGP starts to be collected by the UDR. On the other hand, some carriers in the rear edge of the AGP are trapped because of the very small values of E there. Hence, J_I will have a small dip at $\Theta=270^o$. The premature collection of the AGP is partially completed at $\Theta=288^o$. The edge of the UDR arrives at X=3.4 μm in the diode. Electrons whose density is equal to the background doping density will fill this portion of the DR. Since these carriers are moving in the same direction of the AGP, they contribute to the increase of J_I. The carriers injected into the DR from the ohmic contact are now returning to this contact. Two mechanisms are now affecting J_I in competitive directions. The increase of E causes J_I to increase whereas the extraction of carriers tends to decrease J_I . The induced current will have a peak at $\Theta=297^o$, after which the extraction of carriers becomes the dominant mechanism. The extraction of carriers causes J_I to decrease sharply after this phase angle. This is because the extraction occurs at velocities greater than v_s.

4 Analysis of the Effects of the DC Bias current

As J_{dc} is increased the number of carriers generated by the avalanche process and injected into DR increases. This effect is illustrated in figures 18 through 20. Figure 18 shows J_i and V_t for different Θ at different values of J_{dc}. Figures 19 and 20 show the distribution of the hole current (J_p) and E for different Θ at J_{dc}=1000 and 4000 A/cm^2. The other

operating conditions are F=13 GHz, and P=55 V. It is seen that the height of the avalanche-generated packet (AGP) of holes increases with J_{dc}. This causes the hump of J_i occurring near $\phi=180^o$ to increase with J_{dc}. This effect improves the performance since the number of carriers contributing to the power generation mechanism increases. Consequently, P_{RF} increases with J_{dc} as figure 9 shows. Also η increases firstly with J_{dc} as the same figure shows.

On the other hand, as J_{dc} is increased, the space charge effect (SCE) becomes more pronounced. This effect causes E behind the AGP to increase and that in the front of it to decreases. The depression of the field behind the AGP reduces the phase delay provided by the avalanche process. Hence, this effect causes the performance to be degraded for the high value of J_{dc}. However, the increase of E in front of the AGP either reduces or totally suppresses the drift-velocity dropping below saturation (VDBS) and the DWM effects. Consequently, the optimum value of P increases with J_{dc}. The DWM effect is responsible for the dip occurring in J_i at $\Theta \cong 270^o$. As J_{dc} is increased, this dip is removed because of the suppression of the DWM effect. For higher values of J_{dc}, E will have a second peak that is moving in front of the AGP and the minority carriers enhancement effect increases. Hence the performance is degraded. In addition, E behind the AGP is considerably reduced and some carriers will be trapped in the middle of the diode. The trapping of the carriers behind the AGP is illustrated if Figs 19c and 20d which shows J_p and E at $\Theta = 270^o$ for different values of J_{dc}.

5 Analysis of the Effects of the Operating Frequency

For a given IMPATT structure there is an optimum frequency at which the total phase delay provided by the two mechanisms responsible for IMPATT operation is about 180° [14-17]. These two mechanisms are essentially the avalanche mechanism and the transit-time mechanism.

If the frequency is increased above its optimum value, the time available for the extraction of the AGP will be smaller and a higher number of carriers will still be existing in the DR during the last portion of the RF cycle. Consequently, J_i will be higher as F is increased during this portion. This effect is illustrated in figures 21 through 23 which show J_i, Jp and E for F=8 and 18 GHz. The performance from this point of view is improved. On the other hand, the number of carriers still existing in the far end of the DR at the beginning of the RF cycle will be higher for higher frequencies. Consequently, the power dissipation increases and the avalanche process will start earlier as F is increased. This will reduce the phase delay provided by the avalanche process and increase the spread of transit times of carriers. These effects cause the performance to be degraded as F increases.

On the other hand, as F is decreased below its optimum value, the time during which V_t exceeds the breakdown level increases. This allows the AGP to attain higher values. Consequently, J_i will attain a higher hump at $\Theta \cong 180^o$ as F is increased. This is shown in figure 21. The performance from this point of view is improved. The increase of the size and height of the AGP is attributed to the SCE, which becomes more pronounced as F is increased [21-22]. However, the carriers are extracted early in the cycle and J_i drops significantly during the negative half cycle. Hence, the performance is degraded. In addition, the dc breakdown voltage decreases as F is decreased. Consequently, for the same value of P, the DWM effect becomes more significant as is decreased as it is shown in figures 21 and 22.

6 Conclusions

In this paper, the anomalous behavior of the LHL IMPATT amplifiers is described and interpreted physically. It was indicated that the anomalous increase of gain and output power for these amplifiers are caused by the variation of the mode of operation of the IMPATT. In the region of the sharp increase of gain and power, the IMPATT is operating according to the high-efficiency modes. The n-type IMPATT will operate according to the first high-efficiency mode if the peak of the RF voltage is increased. In this mode, the values of the field in the portion of the DR occupied by the AGP lie in the NDMR of the velocity-field characteristic of the n-type Ga As material. Hence, the AGP of electrons will be bunched and accelerated. Consequently, the induced current will have a peak rather than a dip near the terminal-voltage minimum and the performance is improved. The AGP will be prematurely collected if the peak is increased slightly. During the last quarter of the RF cycle, the electrons injected from the ohmic contact during the DWM will contribute positively to the induced current. This effect gives rise to a second peak in the induced current. Correspondingly, the performance will be

improved. All these factors cause the extraction of the carriers to be more complete in the NHC. This gives rise to the performance improvement through reducing the dc-power dissipation.

Concerning the effects of the dc bias current on the P-type IMPATT it is concluded that: As J_{dc} increases the number of carriers that can contribute to the RF power generation increases. This improves the performance. On the other hand, the SCE increases with J_{dc}. This effect improves the performance through suppressing or at least reducing the VDBS and the effects. In addition, the optimum value of the peak of the RF voltage increases. However, as the SCE becomes more pronounced, the phase delay caused by the avalanche process is reduced, the generation of the minority carriers in the DR is enhanced, and the carrier trapping behind the AGP during the negative half cycle becomes more significant. All these effects cause the performance to be degraded as J_{dc} is increased.

The following conclusions concerning the effects of the operating frequency on the performance are drawn:

For each IMPATT structure, there is an optimum frequency at which the total phase delay provided by the mechanism responsible for IMPATT operation is around 180°. For a higher frequency a greater number of carriers will be extracted at the beginning of the RF cycle. This increases the power dissipation and reduces the phase delay provided by the avalanche process. In addition, the AGP will be wider. All these effects degrade the performance.

If the frequency is lower than the optimum one, the carriers will be extracted early and J_i decreases during the negative half cycle. This degrades the performance. Furthermore, the space charge effect becomes more pronounced as F is decreased.

References

[1] P. Bauhahn and G. I. Haddad, " IMPATT device simulation and properties, " IEEE Trans. Electron Devices, vol. ED-24, Jan., 1977.

[2] C. Bozler et al., "High-efficiency ion-implanted lo-hi-lo GaAs IMPATT diodes,"Appl. Phys. Lett., vol. 29, no. 2, July 15, 1976.

[3] Mukherjee, Moumita; Mazumder, Nilraton; Sitesh Kumar Roy,; Goswami, Kushalendu, " GaN IMPATT diode: a photo-sensitive high power terahertz source", Semiconductor Science and Technology, Volume 22, Number 12, December 2007 , pp. 1258-1267(10)

[4] Y. Hirachi et al., " A new concept for high-efficiency operation of high-low type GaAs IMPATT diodes," IEEE Trans. Electron Devices, vol. ED-25, June 1978.

[5] Hosny A. El-Motaafy , " A new physical explanation for the high-efficiency mode of operation of GaAs IMPATT diodes, " Seventh Conference on Solid-State Science, April, 1984.

[6] Moumita Mukherjee, Nilratan Mazumder, and Sitesh Kumar Roy, " Prospects of 4H-SiC Double Drift Region IMPATT Device as a Photo-Sensitive High-Power Source at 0.7 Terahertz Frequency Regime", Active and Passive Electronic Components , Volume 2008 (2008), Article ID 275357, 9 pages.

[7] El-Sayed A. El-Badawy, S.H. Ibrahim, and H. A. El-Motaafy "، Effects of the operating conditions on the performance of IMPATT amplifiers "،Proceedings of the IEEE International Conference on Semiconductor Electronics, Bangi, Malaysia, Nov., 1998.

[8] Claus J. Schoellhorn, M. Morschbach, H. Xu, W. Zhao and E. Kasper, Associate Member,IEEE, " S-Parameter Measurements of the Impedance of mm-Wave IMPATT Diodes in Dependency on the Current Density", Journal of Microwaves and Optoelectronics, Vol. 3, N.o 5, July 2004, ISSN 1516-739981.

[9] El-Sayed A. El-Badawy, S.H. Ibrahim, and H. A. El-Motaafy," Effect of the Variation of the Doping Densities on the Performance of High Efficiency LHL In P IMPATT Diodes", 1997, IEEE AP-S International Symposium and URSI North American Radio Science Meeting, Montreal, Canada, July 15-18,1997

[10] MoumitaMukherjee,1 Nilratan Mazumder,2 and Sitesh Kumar Roy3," Prospects of 4H-SiC Double Drift Region IMPATT Device as a Photo-Sensitive High-Power Source at 0.7 Terahertz Frequency Regime ", Hindawi Publishing Corporation, Active and Passive Electronic Components, Volume 2008, Article ID 275357, 9 pages.

[11] H. El-Motaafy , El-Sayed A. Badawy, and S.H Ibrahim, "Analysis of Low High-Low InP IMPATT reflection amplifiers", ANTEM'98, Symposium on Antenna and applied electromagnetic, Aug. 1998, Ottawa, Ontario, Canada.

[12] R. L. Kuvas, " Carrier transport in the drift region of Read-type diodes, " IEEE Trans. Electron Devices, vol. ED-25, June 1978.

[13] D. E. Iglesias et al., " 10 W and 12 W GaAs IMPATT's, " IEEE Trans., Electron Devices, vol. 22, no. 4, Apr. 1975.
[14] K. Mouthan, " Two frequency operation of the avalanche-transit-time oscillators, " Proc. IEEE(Lett.), vol. 58, March, 1970.
[15] W. E. Schroeder and G. I. Haddad, " Effect of harmonic and subharmonic signals on avalanche diode oscillator performance, " IEEE Trans. Microwave Theory Tech., vol.MTT-18, June, 1970.
[16] Robert E. Collin," Foundations of Microwave Engineering", McGraw-Hill, 1992.
[17] J.Anaslassiades et al, " Solid-State Microwave Generators", Chapman & Hall, 1992.
[18] D.Christiansen, C.K.Alexander, and R.K. Jurgen , " Standard handbook of Electronic Engineering (5th edition), McGraw Hill, 2006, ISBN 0-07-138421-9
[19] Alexander M. ZEMLOAK, Carlos CELAYA-BORGES, and Roque De La CRUZ," Nonlinear Analysis of Double Avalanche Region IMPATT Diode", IEICE TRANS. ELECTRON., VOL. E88-C, No. 1 January 2005.
[20] H. El-Motaafy, " Full-scale computer simulation of TRAPATT diodes, " The Third National Radio-Science Symposium, Cairo, 1985.
[21] S.H. Ibrahim, El-Sayed A. El-Badawy, and H. A. El-Motaafy," Effect of the Operating Conditions on the performance of high Efficiency In P IMPATT Diodes," International Wireless Telecommunications Symposium / Exhibition, May 14-16, 1997 Shah Alam, Malaysia.
[22] S. Selberherr, " Analysis and simulation of semiconductor devices," Springer-Verlag Wien New York, 1984.

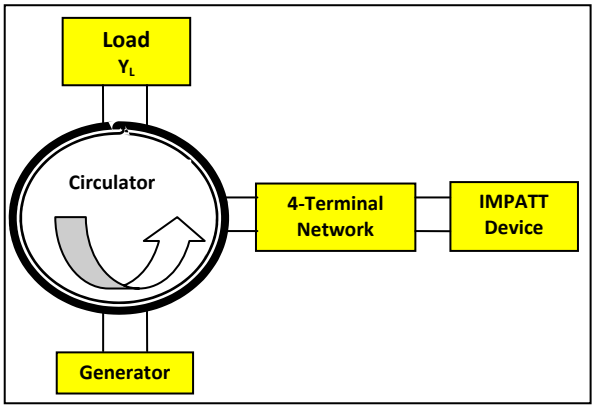

Fig. 1: Reflection Amplifier configuration

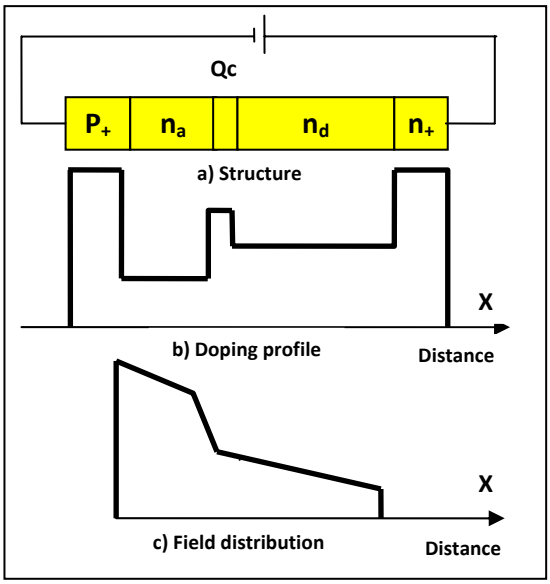

Fig. 2: LHL structure of IMPATT Diode

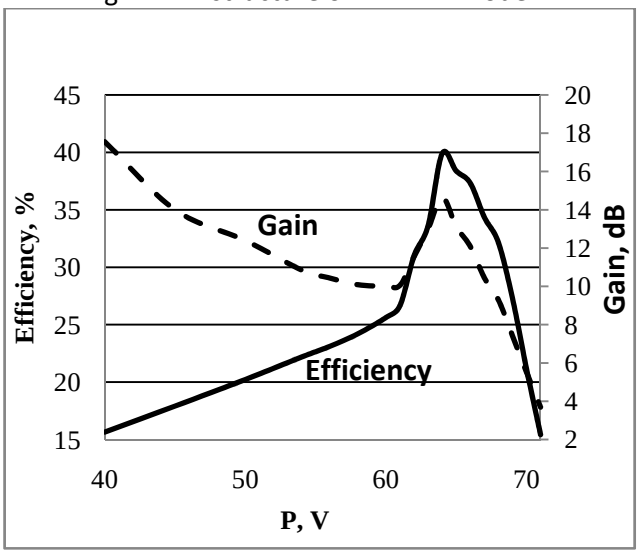

Fig.3: Efficiency and gain versus the peak voltage (P)

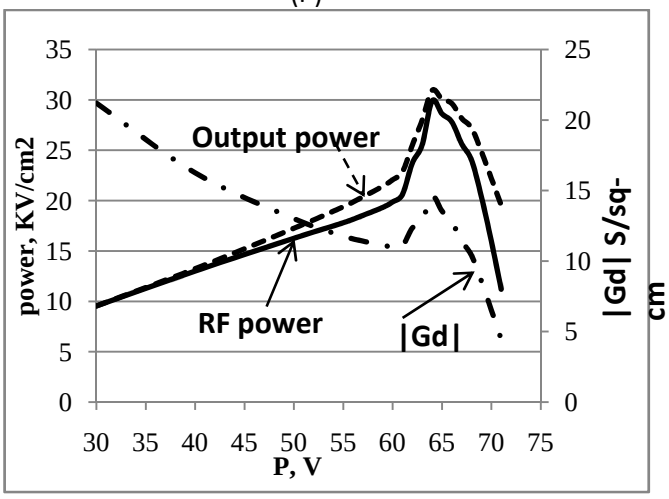

Fig. 4: The magnitude of the diode conductance, $|G_d|$, the RF power and the output power versus the peak voltage (P)

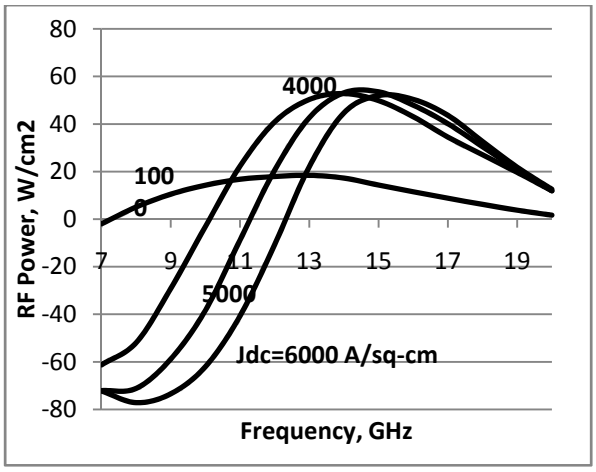

Fig. 5: The RF Power (P_{RF}) versus frequency for dc bias current ranging from 1000 A/cm^2 to 6000A/cm^2

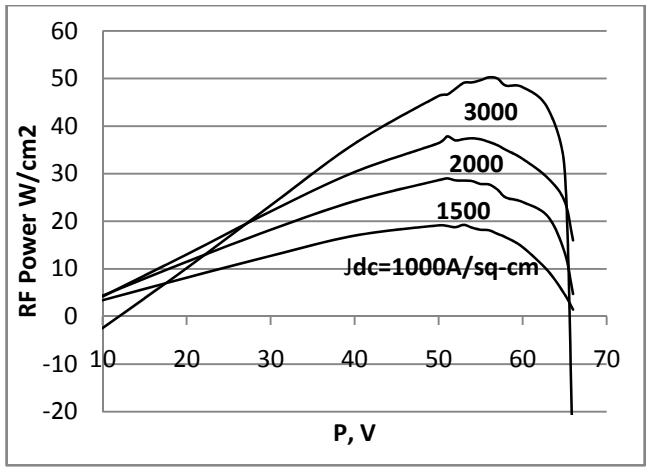

Fig. 8 The RF Power (P_{RF}) versus terminal voltage (P) for dc bias current ranging from 1000 A/cm^2 to 3000A/cm^2

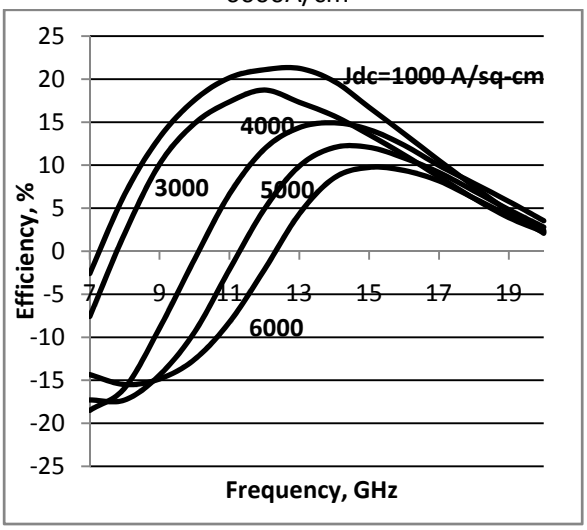

Fig. 6: The Efficiency versus frequency for dc bias current ranging from 1000 A/cm^2 to 6000A/cm^2

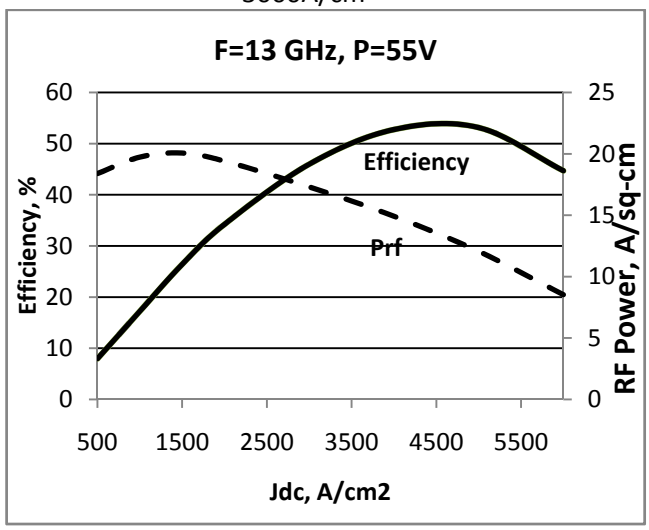

Fig. 9: The RF Power (P_{RF}) and efficiency versus dc bias current (J_{dc})

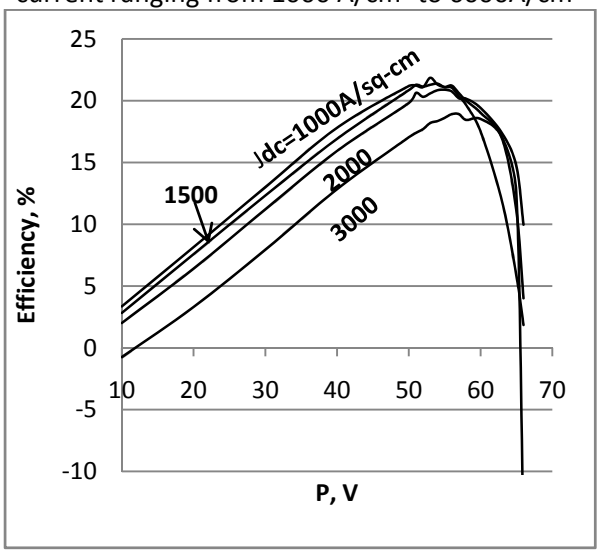

Fig. 7: The efficiency versus terminal voltage (P) for dc bias current ranging from 1000 A/cm^2 to 3000A/cm^2

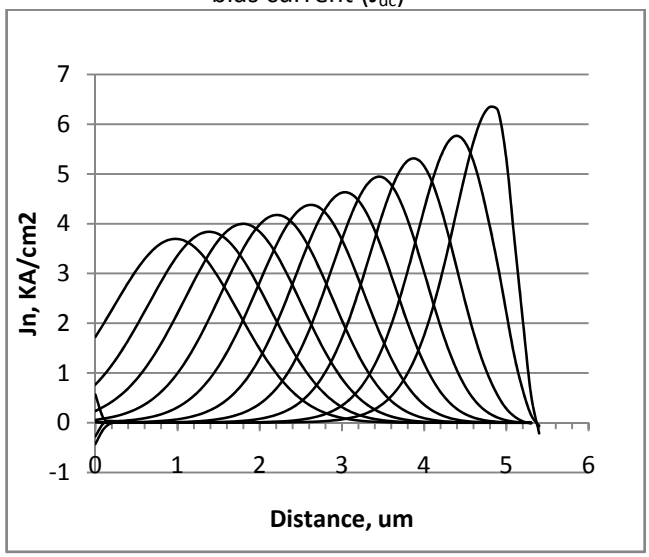

Fig. 10 : The electron current density (J_n) versus distance at P=45 V

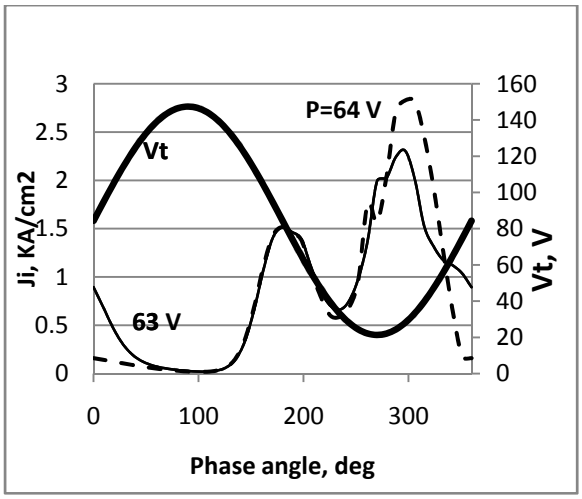

Fig.11: The induced current (J_i) and the terminal voltage (Vt) for P=63 and 64 V

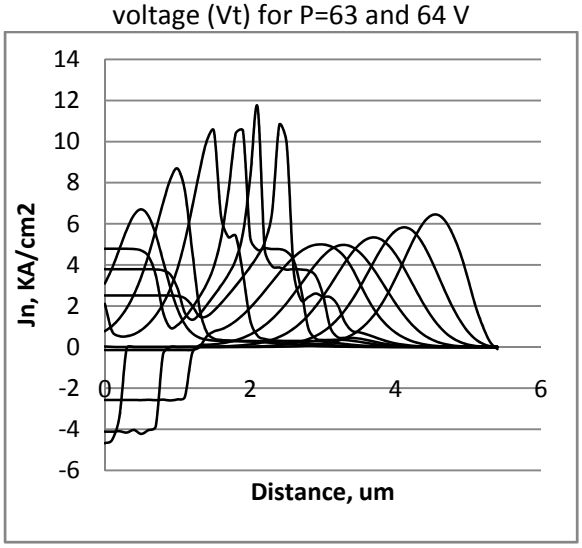

Fig. 12: The electron current density (J_n) for P=63 V

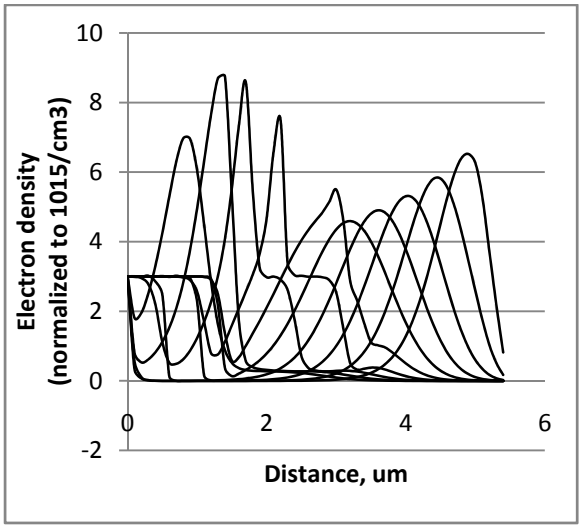

Fig. 13: The electron density for P=63 V

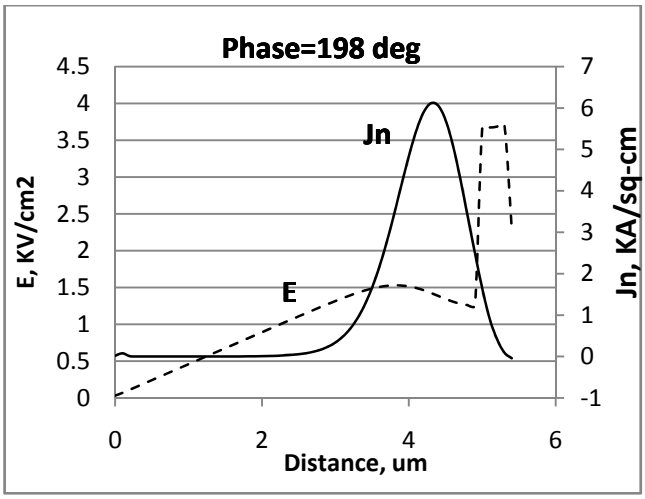

Fig. 14a: J_n and electric field (E) at θ=198^0 and P=63 V

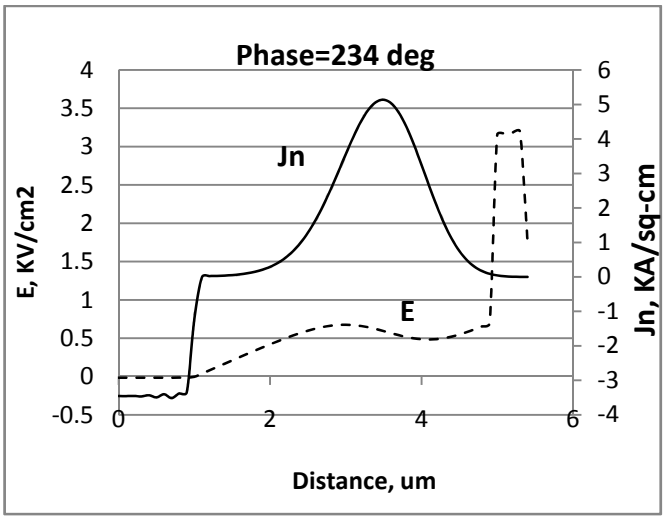

Fig. 14b: The electron current density (J_n) and electric field (E) at θ=234^0 and P=63 V

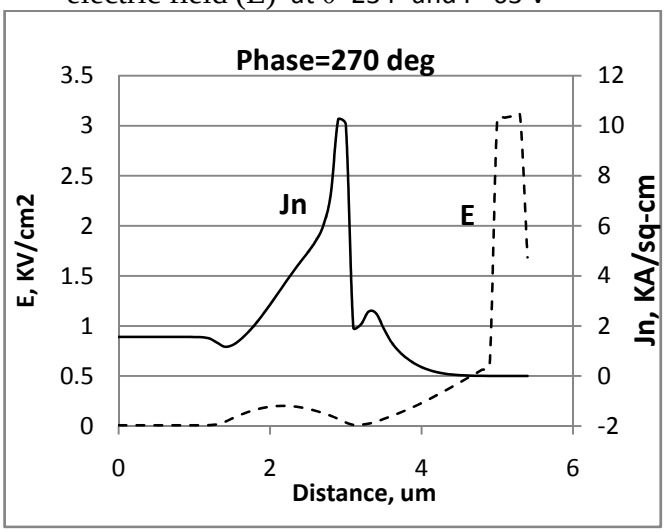

Fig. 14c: The electron current density (J_n) and electric field (E) at θ=270^0 and P=63 V

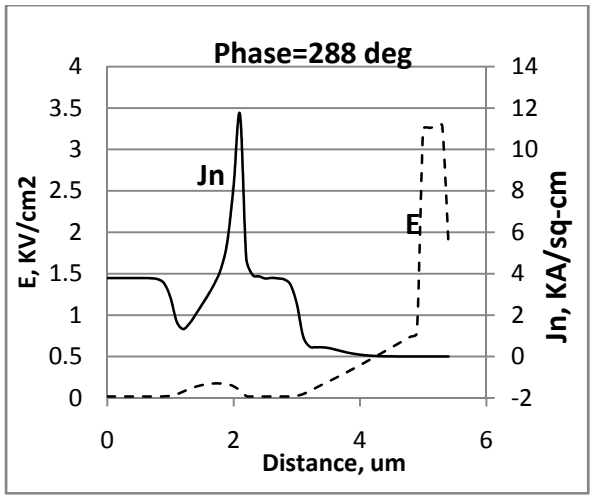

Fig. 14d: The electron current density (J_n) and electric field (E) at $\theta=288^0$ and P=63 V

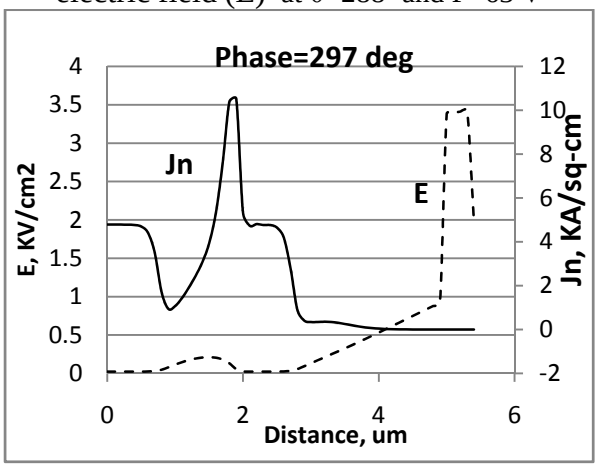

Fig. 14e: The electron current density (J_n) and electric field (E) at $\theta=297^0$ and P=63 V

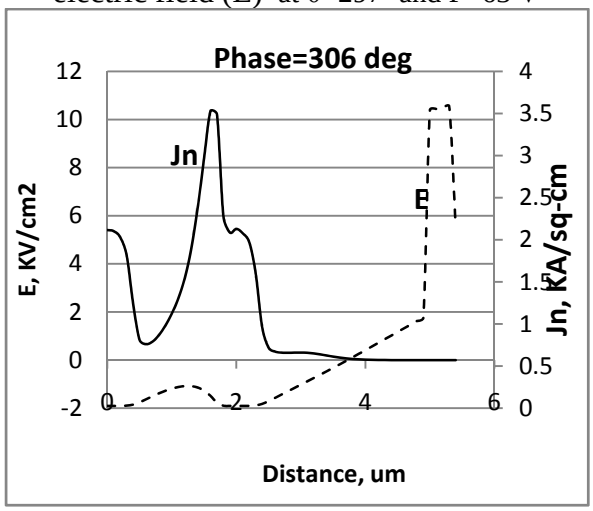

Fig14f: The electron current density (J_n) and electric field (E) at $\theta=306^0$ and P=63 V

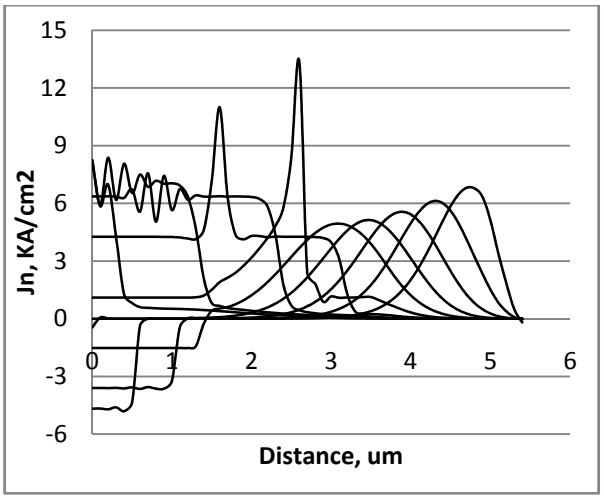

Fig. 15: The electron current density(J_n) for P=64 V

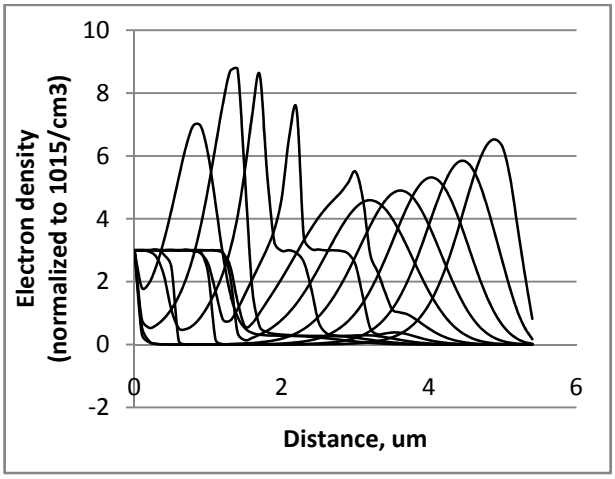

Fig. 16: The electron density for P=64 V

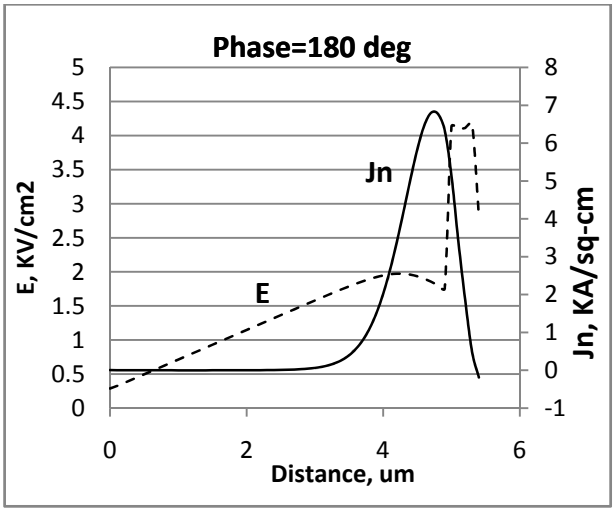

Fig. 17a: The electron current density (J_n) and electric field (E) at $\theta=180^0$ at P=64 V

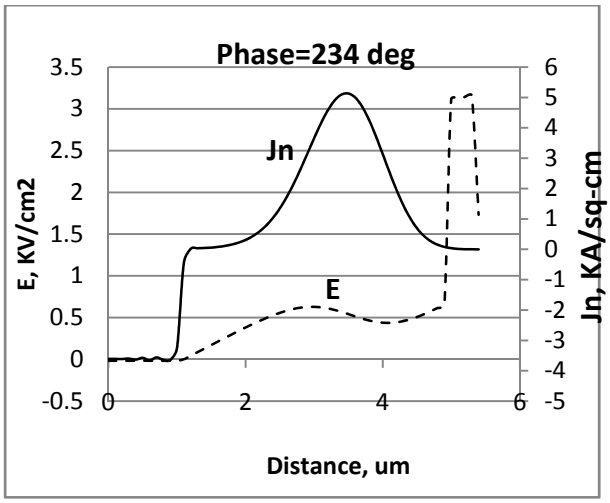

Fig. 17b: The electron current density (J_n) and electric field (E) at $\theta=234^0$ at P=64 V

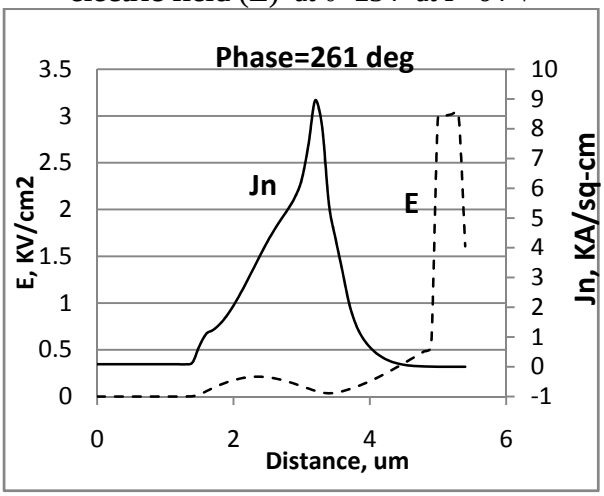

Fig. 17c: J_n and electric field (E) at $\theta=261^0$ at P=64 V

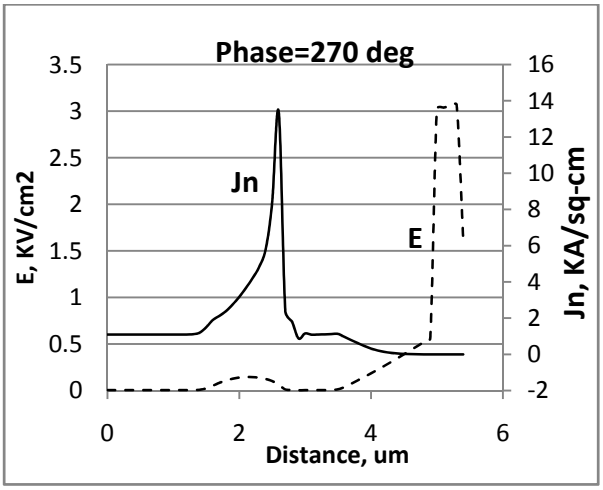

Fig. 17d: The electron current density (J_n) and electric field (E) at $\theta=270^0$ at P=64 V

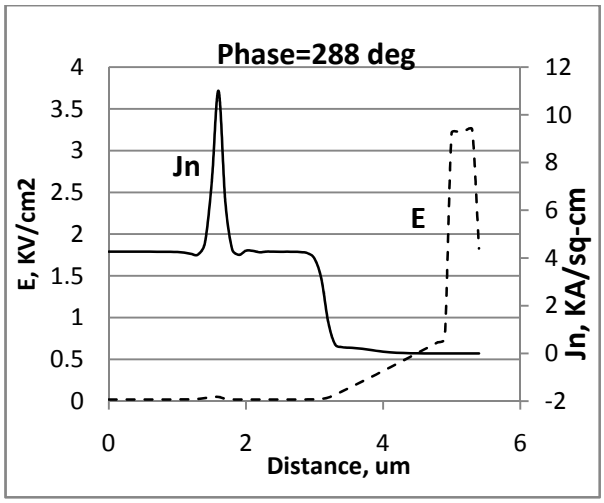

Fig. 17e: The electron current density (J_n) and electric field (E) at $\theta=288^0$ at P=64 V

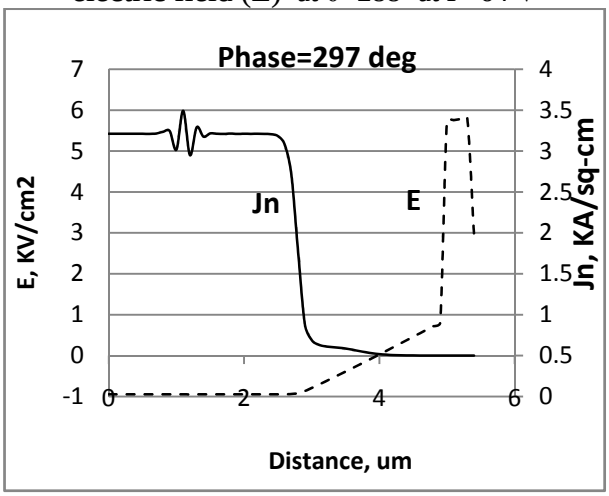

Fig. 17f: The electron current density (J_n) and electric field (E) at $\theta=297^0$ at P=64 V

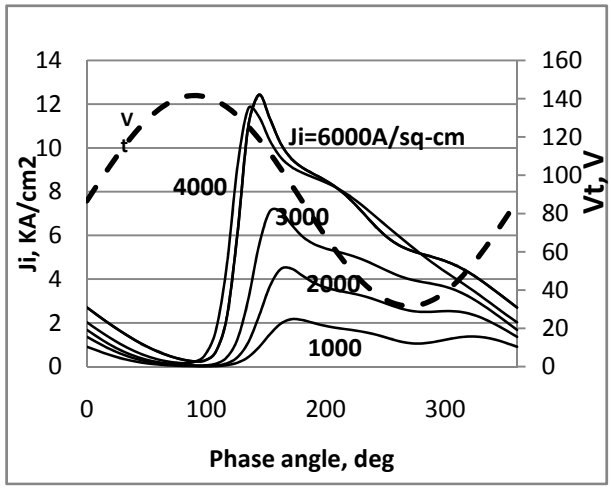

Fig. 18: The induced current (J_i) and the terminal voltage, (V_t) for dc current (J_{dc}) values ranging from 1000 to 6000 A/cm^2

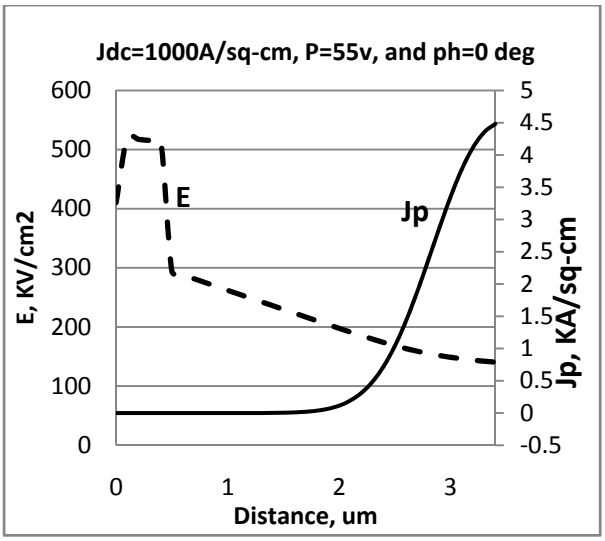

Fig. 19a

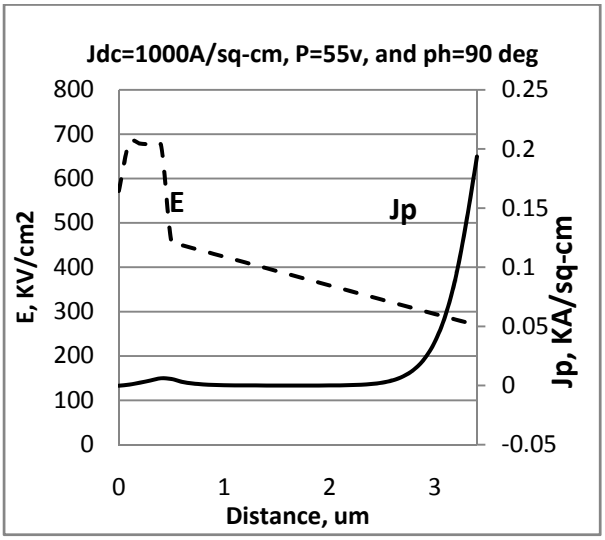

Fig. 19b

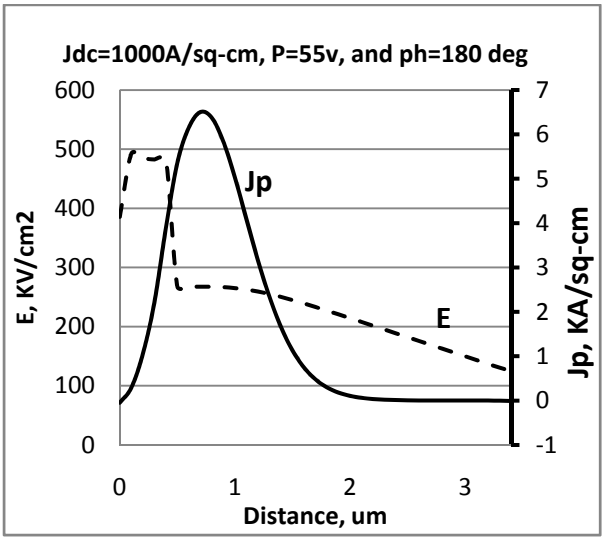

Fig. 19c

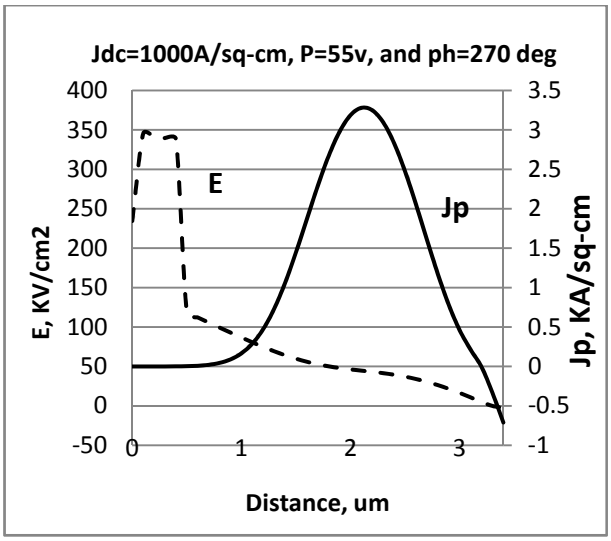

Fig. 19c:

Fig. 19: The spatial distribution of the hole current (J_P) and the electric field (E) at J_{dc}=1000 A/cm^2 for different phase angles

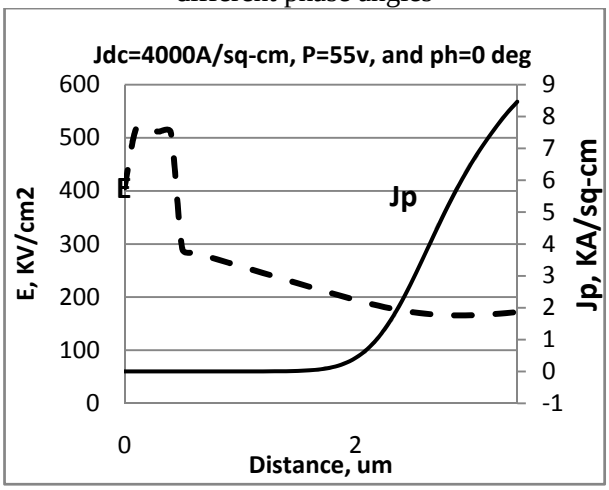

Fig. 20a

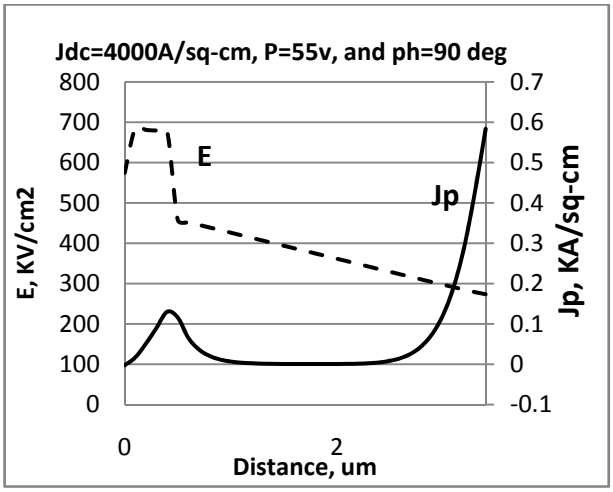

Fig. 20b

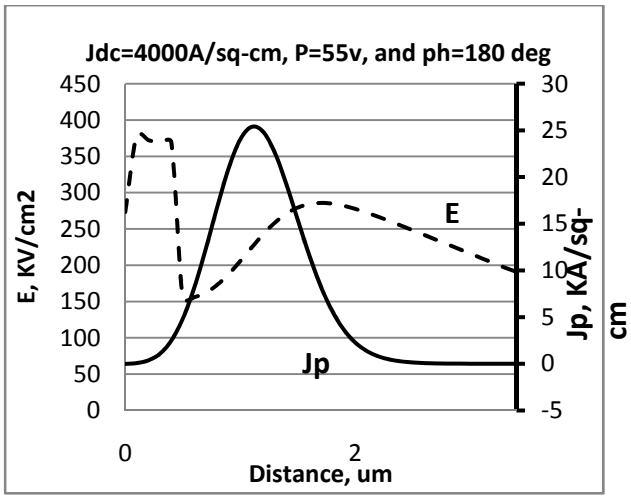

Fig. 20c

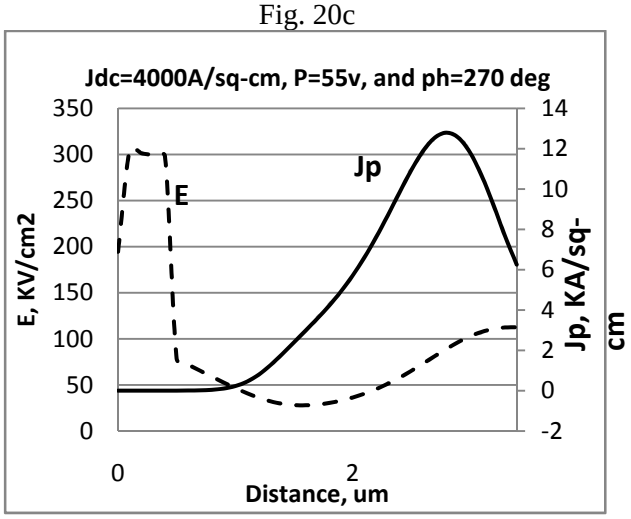

Fig. 20d

Fig. 20: The spatial distribution of the hole current (J_P) and the electric field (E) at J_{dc}=4000 A/cm^2 for different phase angles

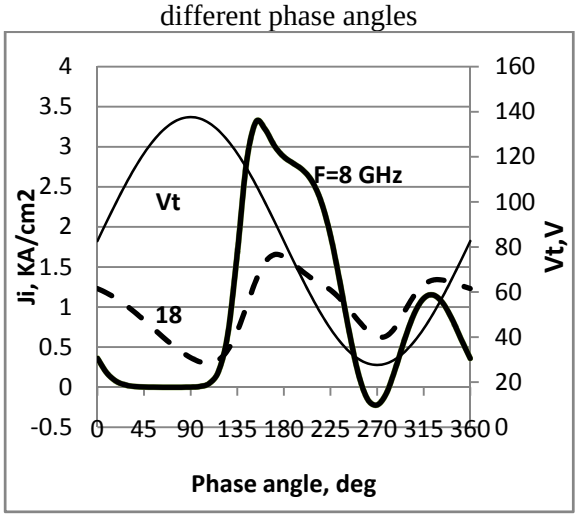

Fig. 21: The induced current (J_i) and the terminal voltage, (V_t) for different values of the frequency (F)

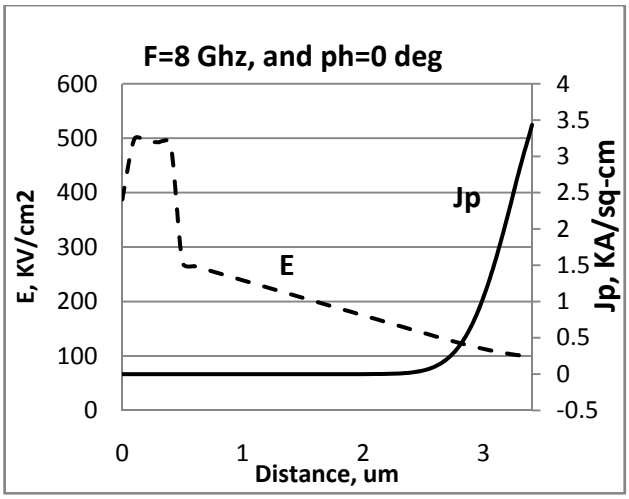

Fig. 22a

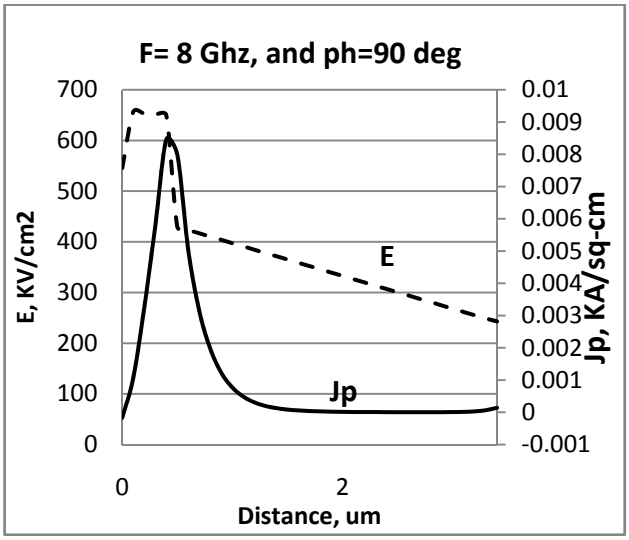

Fig. 22b

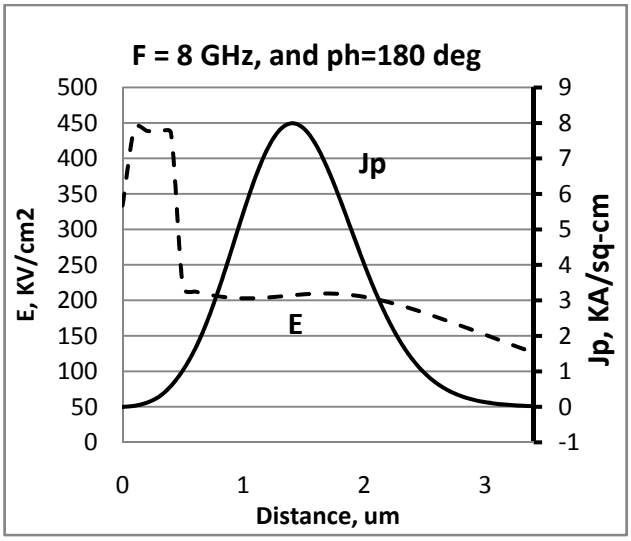

Fig. 22c

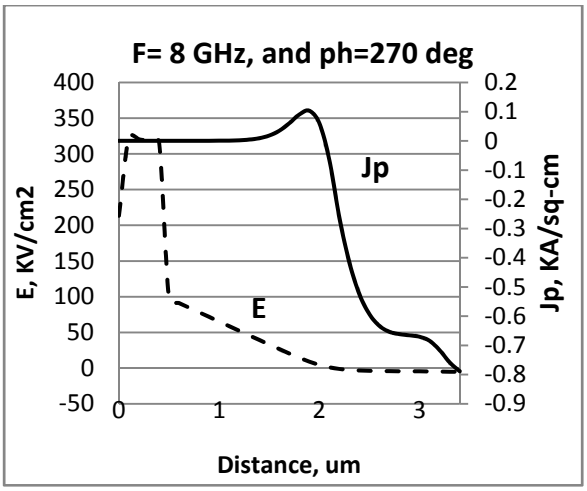

Fig. 22d

Fig. 22: The spatial distribution of the hole current (J_P) and the electric field (E) at F=8 GHz for different phase angles

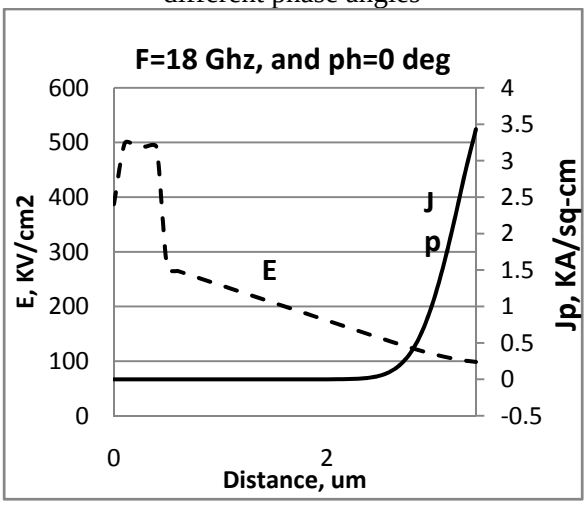

Fig. 23a

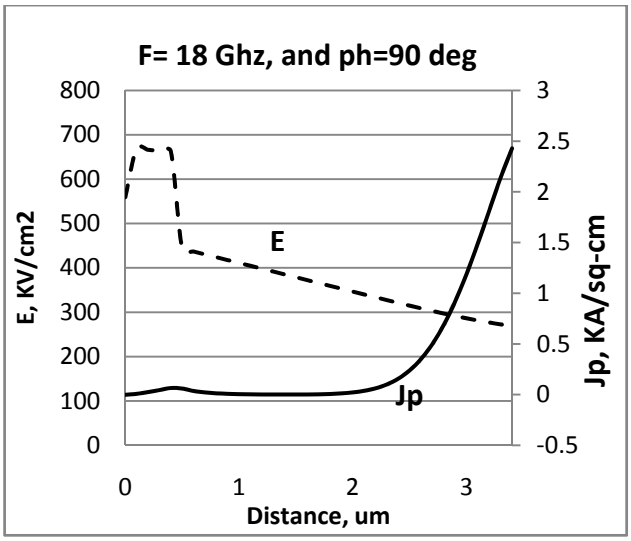

Fig. 23b

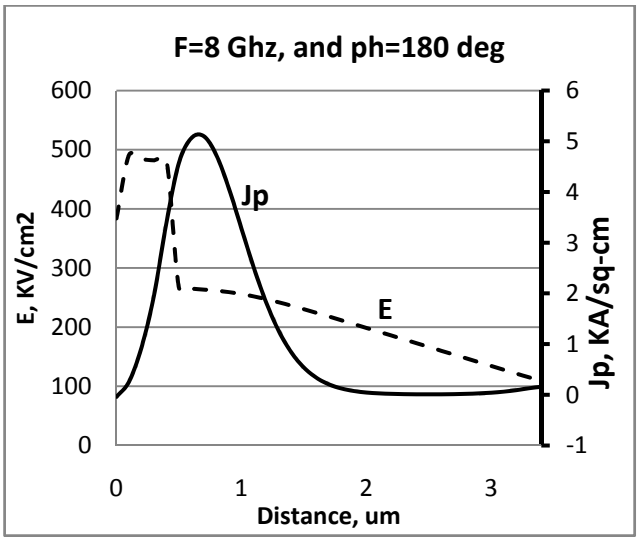

Fig. 23c

Fig. 23: The spatial distribution of the hole current (J_P) and the electric field (E) at F=18 GHz for different phase angles